Article

Differentiator-Based Output Feedback MPPT Controller for DFIG Wind Energy Conversion Systems with Minimal System Information

Jang-Hyun Park

Department of Electrical and Control Engineering, Mokpo National University,
Chonnam 58554, Republic of Korea; jhpark72@mokpo.ac.kr

Abstract: This paper introduces a novel differentiator-based maximum power point tracking (MPPT) controller for a wind energy conversion system (WECS) equipped with a doubly fed induction generator (DFIG). Building upon our previous algorithms, the proposed controller reduces the need for detailed system information and displays enhanced robustness against parameter variations and disturbances. The innovation lies in the elimination of the need for explicit functional forms or specific parameter values in the system's dynamics, relying solely on relative degrees and control directions. Utilizing a higher-order switching differentiator (HOSD), this paper outlines a method for overestimating the time derivatives of system outputs, thereby simplifying both the controller design and stability analysis. Compared to existing solutions, the proposed method requires minimal information, offers simpler control law structures, and follows a systematic design approach with fewer design constants. Simulation results demonstrate the efficacy of the proposed controller in both tracking maximum power and regulating reactive power to zero, suggesting a more efficient and simplified approach to MPPT control in WECS.

Keywords: wind energy conversion system; differentiator-based controller; doubly fed induction generator

1. Introduction

Due to concerns surrounding pollution, high costs, potential depletion, and other adverse impacts associated with traditional energy sources, renewable energy generation has garnered substantial interest. Among the various renewable energy technologies, the wind energy conversion system (WECS) stands out as one of the most developed and widely used, primarily because it is clean, inexhaustible, and broadly accessible. Furthermore, the doubly fed induction generator (DFIG) is deemed as a stable and efficient fixed-speed wind turbine system [1,2]. With its lower converter cost and reduced power losses, the DFIG has attracted considerable attention from numerous researchers.

While the conventional Proportional–Integral (PI) controller exhibits satisfactory performance across numerous WECS applications, efforts have been made to enhance WECS performance through the introduction of optimized PI controllers [3,4]. However, these controllers exhibit limitations, notably their inability to adapt to variations in machine parameters and uncertainties. Therefore, any deviation in operational conditions from those under which the PI controller parameters were optimized cannot assure optimal operation. This necessitates real-time PI controller parameter tuning in response to wind speed variations and potential parametric alterations, often due to technical complications such as mechanical wear or machine overheating. In a practical sense, implementing these techniques remains challenging and costly. The difficulties largely stem from determining the optimal gains of the controller needed to achieve control objectives across all operating regions and to adapt well to changes in system parameters. These shortcomings inherent in PI or optimized PI controllers have prompted the development and implementation

of robust and adaptive control techniques for WECS. Proposals have been put forth for more robust control strategies to supplant PI controllers in order to enhance precision and accuracy performance [5].

Inherently, WECS exhibit strongly nonlinear dynamic equations. Furthermore, their system parameters are prone to variations due to factors such as ambient temperature changes and mechanical wear. Conventionally, the design of stabilizing controllers for nonlinear systems characterized by unstructured uncertainties including parameter variations and external disturbances have largely leveraged sliding mode control (SMC) methods [6,7] and adaptive control algorithms with universal approximators such as neural networks (NN) or fuzzy logic systems (FLS) [8–16]. Although these NNs and FLS approximators have found wide application in addressing system uncertainties, they require a complex structure to ensure approximation capabilities. Furthermore, they necessitate the online updating of a multitude of adaptive parameters, thereby leading to a heightened computational load and dynamic order of the controller. Recently, control strategies aiming to simplify complex control formulas without compromising their performance have been proposed. This includes prescribed performance control (PPC) techniques that guarantee a predefined tracking performance irrespective of system uncertainties, and without the need for approximation [17–20]. The PPC framework significantly simplifies the controller structure by eliminating the need for universal approximators. Yet, the steps of the backstepping design continue to be an integral part of PPC methodologies, making them vulnerable to faults or large disturbances after the transient period. More recently, the proposal of differentiator-based controllers emerged, which address system uncertainties by overestimating the time derivatives of the output tracking error, eliminating the need for universal approximations [21,22]. Despite the surge in research in this field, a large proportion of the studies target single-input single-output (SISO) nonlinear systems, leaving multi-input multi-output (MIMO) systems relatively under-explored.

Recently, SMC methods have been applied to maximum power point tracking (MPPT) control of WECS [23,24]. However, these control strategies are constructed under the assumption that both the formulas and parameters of system dynamics are fully known, in order to cancel out the system's nonlinearities, making this approach somewhat restrictive. To alleviate these restrictions, adaptive fuzzy or neuro-controllers are introduced in [25–30]. While these control techniques, which are based on universal approximators, offer the benefit of not necessitating prior knowledge about the nonlinear functions in the system's dynamic equation, they come with the complexity of intricate control laws and formulas for updating adjustable parameters. This complexity poses significant challenges for the actual implementation of the control algorithm. In [31,32], the PPC schemes are utilized for MPPT control of WECS. Nonetheless, the PPC algorithm is susceptible to faults or abrupt disturbances that manifest in a steady state. In this paper, building upon the control algorithm presented in [21,22], we propose a novel differentiator-based MPPT controller for WECS equipped with DFIG. The advantage of the proposed controller is twofold: it obviates the need for information about the nonlinear functions present in the system's dynamic equation, and it can adeptly handle both parameter variations and disturbances. When designing the controller, we assume that the time derivatives of outputs are aggregated unknown functions of the inputs and time. Consequently, apart from information regarding relative degrees and control direction, specific functional expressions and parameter values of the system dynamics are not considered in the controller's formulation. Employing HOSD [33], we over-estimate the time derivatives of the system outputs, facilitating both a more streamlined controller structure and a more straightforward stability analysis. The advantages of the controller presented in this paper, relative to existing research, are as follows:

1. The proposed controller demands significantly less information about the system's dynamic equation. The control formulation relies solely on the relative degrees between inputs and outputs, the directions of control inputs, and the measured output values.

2. Owing to the absence of universal approximators, the structures of the control laws are comparatively straightforward, while still ensuring the asymptotic stability of the outputs.

3. The proposed output feedback control algorithm offers a cohesive and systematic approach for crafting control laws.

4. The quantity of design constants is minimal in comparison to that of other methods.

Simulation results are provided to showcase the efficacy of the proposed controller and the consistency inherent in its design.

The organization of this paper is as follows. Section 2 provides the dynamic equations for DFIG-WECS and derives the state equations. Section 3 introduces a differentiator-based output feedback MPPT controller. Section 4 presents simulation results, including a comparison of the performance between the proposed controller and a conventional PI controller. Finally, Section 5 offers conclusions. The symbols used in describing the DFIG-WECS and their meanings in this paper are summarized in Table 1.

Table 1. Symbols of DFIG-WECS.

Notation	Description
$v_w(t)$	wind speed
J_t	inertia of the turbine
J_g	inertia of the generator
n_g	gear ratio
J	total inertia ($= J_t + n_g^2 J_g$)
D	damping constant of the wind turbine
ρ	air density
R	radius of the blade
A	the area swept by the blades
$\omega(t)$	rotational velocity of the wind turbine's rotor
$\lambda(t)$	tip-speed ratio ($= \omega R / v_w$)
λ^*	optimal value of tip-speed ratio λ
β	blade pitch angle
$C_p(\lambda, \beta)$	power coefficient function defined as (3)
$c_1, \cdots, c_6$	system constants in the $C_p(\lambda, \beta)$ function
ω_s	stator electrical angular speed
R_s	stator resistance
R_r	rotor resistance
L_s	stator inductance
L_r	rotor inductance
L_m	mutual inductance
p_r	number of pole pairs
$i_{rd}(t), i_{rq}(t)$	d- and q-axis currents of the generator's rotor
$v_{rd}(t), v_{rq}(t)$	d- and q-axis voltages of the generator's rotor
$\phi_s(t)$	d-axis flux of the generator's stator
$P_s(t), Q_s(t)$	active and reactive powers

2. Dynamic Model of the WECS with DFIG

2.1. Model of WECS

The mechanical power generated by the wind turbine is described by equation

$$P_t = \frac{1}{2} \rho A C_p(\lambda, \beta) v_w^3, \tag{1}$$

where ρ is the air density, A is the area swept by the blades, $C_p(\lambda, \beta)$ is the power coefficient, λ is the tip speed ratio, β is the blade pitch angle, and v_w is the wind speed. The tip speed ratio is defined as

$$\lambda = \frac{v_t}{v_w} = \frac{\omega R}{v_w}, \tag{2}$$

where v_t is the tip speed of the blade, ω is the rotational velocity of the wind turbine's rotor, and R is the radius of the blade. The conceptual diagram illustrating these parameters is depicted in Figure 1.
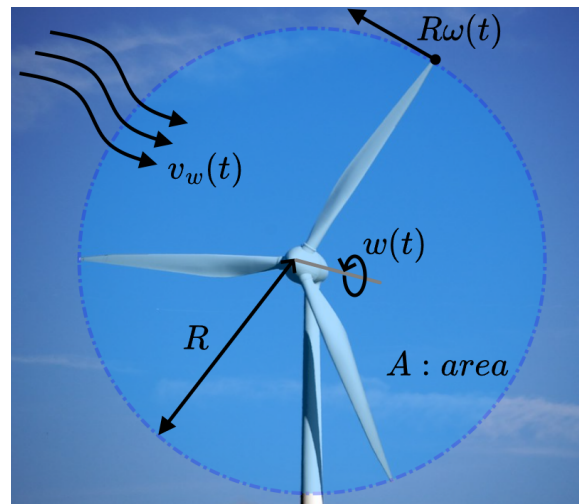

Figure 1. Concept diagram of the paramters.

The power coefficient serves as a metric for quantifying the efficiency of the wind turbine in converting the kinetic energy of the wind into mechanical energy. It is defined as the ratio of the power harnessed by the wind turbine to the total power available in the wind. In this study, we employ the following equation for the power coefficient, as adapted from the literature [34]:

$$C_p(\lambda, \beta) = c_1\left(\frac{c_2}{\lambda_\beta} - c_3\beta - c_4\right)e^{-\frac{c_5}{\lambda_\beta}} + c_6\lambda \tag{3}$$

and

$$\frac{1}{\lambda_\beta} = \frac{1}{\lambda + 0.008\beta} - \frac{0.035}{\beta^3 + 1}. \tag{4}$$

Here, coefficients c_i ($i = 1, \ldots, 6$) are obtained from [34] and are detailed in the simulation section. The aerodynamic torque of turbine T_a is given by equation

$$T_a = \frac{P_t}{\omega} = \frac{1}{2\omega}\rho\pi R^2 C_p(\lambda)v_w^3. \tag{5}$$

The first-order dynamic model of the wind turbine can be expressed as

$$J\dot{\omega} = T_a - D\omega - n_g T_{em}, \tag{6}$$

where J represents the total inertia, which is the sum of the inertia from the turbine and the generator:

$$J = J_t + n_g^2 J_g. \tag{7}$$

J_t is the inertia of the turbine, J_g is the inertia of the generator, n_g is the transmission ratio of the gearbox, D is the damping constant of the wind turbine, and T_{em} is the electromagnetic torque, which is defined subsequently. Overall schematic of the proposed control system is illustrated in Figure 2 and typical power coefficient curves are depicted in Figure 3 for various blade pitch angles.
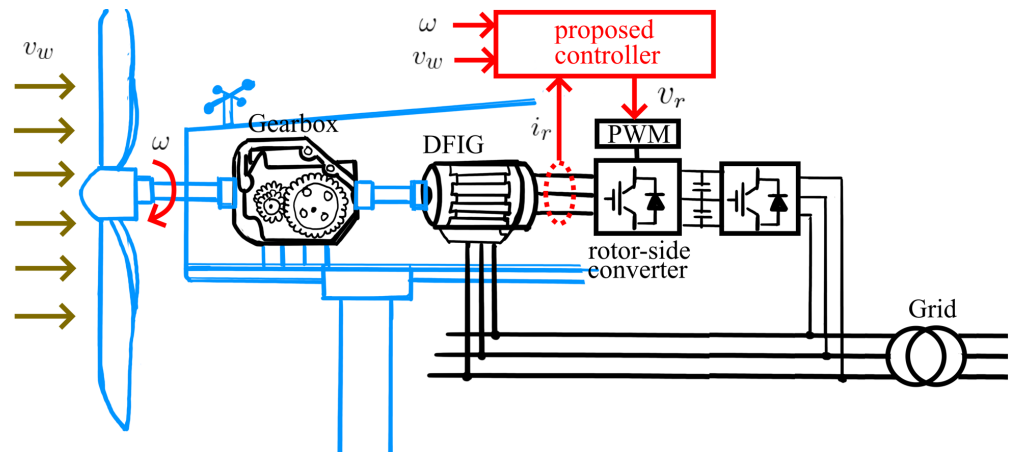
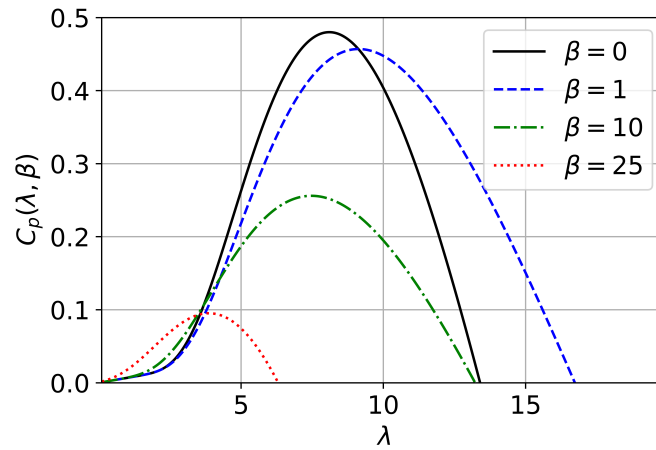**Figure 2.** Overall schematic of the DFIG-based generator side control system.

Figure 3. Typical C_p curves with respect to pitch angle.

At low wind speeds, λ should be maintained at its optimal value λ^* to maximize conversion efficiency. Therefore, the desired rotor speed ω_d can be calculated using the current wind speed as follows:

$$\omega_d = \frac{\lambda^*}{R} v_w. \tag{8}$$

The primary control objective for the WECS under consideration is to ensure that the angular speed of the blade ω tracks the desired value given by Equation (8). This is commonly referred to as MPPT in the subsequent discussion.

2.2. Mathematical Model of DFIG

In the equations that follow, v_{sd}, v_{sq}, v_{rd}, v_{rq}, i_{sd}, i_{sq}, i_{rd}, i_{rq}, ϕ_{sd}, ϕ_{sq}, ϕ_{rd}, and ϕ_{rq} represent the d and q components of the stator and rotor voltages, currents, and fluxes, respectively. The commonly used electrical equations for the DFIG in the Park reference frame are given as follows:

$$v_{sd} = R_s i_{sd} + \frac{d\phi_{sd}}{dt} - \omega_s \phi_{sq}, \tag{9}$$

$$v_{sq} = R_s i_{sq} + \frac{d\phi_{sq}}{dt} + \omega_s \phi_{sd}, \tag{10}$$

$$v_{rd} = R_r i_{rd} + \frac{d\phi_{rd}}{dt} - \omega_r \phi_{rq}, \tag{11}$$

$$v_{rq} = R_r i_{rq} + \frac{d\phi_{rq}}{dt} + \omega_r \phi_{rd}. \tag{12}$$

Here, R_s and R_r denote the resistances of the stator and rotor, respectively. Symbols ω_s and ω_r represent the stator and rotor electrical angular speeds in the synchronous reference

frame. Since the rotor is directly connected to the blade through a gearbox, equation $\omega_r = n_g \omega$ holds true. The dynamics of the stator and rotor fluxes are described by the following equations:

$$\phi_{sd} = L_s i_{sd} + L_m i_{rd}, \tag{13}$$

$$\phi_{sq} = L_s i_{sq} + L_m i_{rq}, \tag{14}$$

$$\phi_{rd} = L_r i_{rd} + L_m i_{sd}, \tag{15}$$

$$\phi_{rq} = L_r i_{rq} + L_m i_{sq}, \tag{16}$$

where L_s and L_r denote the inductances of the stator and rotor, respectively, and L_m represents the mutual inductance. The electromagnetic torque is described by

$$T_{em} = p_r (\phi_{sd} i_{sq} - \phi_{sq} i_{sd}), \tag{17}$$

where p_r is the number of pole pairs. Furthermore, the stator's active and reactive powers are given by

$$P_s = v_{sd} i_{sd} + v_{sq} i_{sq}, \tag{18}$$

$$Q_s = v_{sd} i_{sq} - v_{sq} i_{sd}. \tag{19}$$

The state equations are derived based on the assumption that both stator and rotor variables are referred to the stator reference Park frame [23,34]. Given this orientation, the following relationships hold:

$$\phi_{sd} = \phi_s, \tag{20}$$

$$\phi_{sq} = 0, \tag{21}$$

and

$$v_{sd} = 0, \tag{22}$$

$$v_{sq} = v_s, \tag{23}$$

where ϕ_s represents the total flux and v_s signifies the total voltage of the stator. From these, i_{sd} and i_{sq} can be derived using Equations (13) and (14):

$$i_{sd} = \frac{1}{L_s}(\phi_s - L_m i_{rd}), \tag{24}$$

$$i_{sq} = -\frac{L_m}{L_s} i_{rq}. \tag{25}$$

Utilizing the following equations, which arise from Equations (16) and (25),

$$\frac{d\phi_{rq}}{dt} = L_r \frac{di_{rq}}{dt} + L_m \frac{di_{sq}}{dt}, \tag{26}$$

$$\frac{di_{sq}}{dt} = -\frac{L_m}{L_s} \frac{di_{rq}}{dt}, \tag{27}$$

the dynamic equation for i_{rq} can be derived from Equation (12) as follows:

$$
\begin{aligned}
v_{rq} &= R_r i_{rq} + \frac{d\phi_{rq}}{dt} + \omega_r \phi_{rd} \\
&= R_r i_{rq} + \left(L_r \frac{di_{rq}}{dt} + L_m \frac{di_{sq}}{dt} \right) + \omega_r (L_r i_{rd} + L_m i_{sd}) \\
&= R_r i_{rq} + \left(L_r - \frac{L_m^2}{L_s} \right) \frac{di_{rq}}{dt} + \omega_r \left\{ \left(L_r - \frac{L_m^2}{L_s} \right) i_{rd} + \frac{L_m}{L_s} \phi_s \right\} \\
&= R_r i_{rq} + \sigma L_r \frac{di_{rq}}{dt} + \omega_r \left(\sigma L_r i_{rd} + \frac{L_m}{L_s} \phi_s \right),
\end{aligned}
\tag{28}
$$

where $\sigma = 1 - \frac{L_m^2}{L_r L_s}$, leading to

$$
\frac{di_{rq}}{dt} = -\frac{R_r}{\sigma L_r} i_{rq} - \omega_r \left(i_{rd} + \frac{L_m}{\sigma L_r L_s} \phi_s \right) + \frac{1}{\sigma L_r} v_{rq}.
\tag{29}
$$

Dynamic equation for ϕ_s is induced from (9) using (24) as

$$
\begin{aligned}
\frac{d\phi_s}{dt} &= -R_s i_{sd} \\
&= -\frac{R_s}{L_s} \phi_s + \frac{R_s L_m}{L_s} i_{rd}.
\end{aligned}
\tag{30}
$$

Utilizing the following equations, derived from (15) and (24),

$$
\frac{d\phi_{rd}}{dt} = L_r \frac{di_{rd}}{dt} + L_m \frac{di_{sd}}{dt},
\tag{31}
$$

$$
\frac{di_{sd}}{dt} = \frac{1}{L_s} \frac{d\phi_s}{dt} - \frac{L_m}{L_s} \frac{di_{rd}}{dt},
\tag{32}
$$

the dynamic equation for i_{rd} can be derived from (11) as follows:

$$
\begin{aligned}
v_{rd} &= R_r i_{rd} + \frac{d\phi_{rd}}{dt} - \omega_r \phi_{rq} \\
&= R_r i_{rd} + \left(L_r \frac{di_{rd}}{dt} + L_m \frac{di_{sd}}{dt} \right) - \omega_r (L_r i_{rq} + L_m i_{sq}) \\
&= R_r i_{rd} + \left\{ L_r \frac{di_{rd}}{dt} + L_m \left(\frac{1}{L_s} \frac{d\phi_s}{dt} - \frac{L_m}{L_s} \frac{di_{rd}}{dt} \right) \right\} - \omega_r \left(L_r i_{rq} - \frac{L_m^2}{L_s} i_{rq} \right) \\
&= R_r i_{rd} + \left(L_r - \frac{L_m^2}{L_s} \right) \frac{di_{rd}}{dt} + \frac{L_m}{L_s} \frac{d\phi_s}{dt} + \omega_r \left(L_r - \frac{L_m^2}{L_s} \right) i_{rq} \\
&= R_r i_{rd} + \sigma L_r \frac{di_{rd}}{dt} + \frac{L_m}{L_s} \left(-\frac{R_s}{L_s} \phi_s + \frac{R_s L_m}{L_s} i_{rd} \right) + \omega_r \sigma L_r i_{rq} \\
&= \left(R_r + \frac{R_s L_m^2}{L_s^2} \right) i_{rd} + \sigma L_r \frac{di_{rd}}{dt} - \frac{L_m R_s}{L_s^2} \phi_s + \omega_r \sigma L_r i_{rq}.
\end{aligned}
\tag{33}
$$

This leads to

$$
\frac{di_{rd}}{dt} = -\frac{1}{\sigma L_r} \left(R_r + \frac{R_s L_m^2}{L_s^2} \right) i_{rd} + \omega_r i_{rq} + \frac{L_m R_s}{\sigma L_r L_s^2} \phi_s + \frac{1}{\sigma L_r} v_{rd}.
\tag{34}
$$

The resulting four dynamic equations that constitute the state-space representation of the WECS with DFIG are collected as follows:

$$\frac{d\omega}{dt} = \frac{1}{J}(T_a - D\omega - n_g T_{em}), \tag{35}$$

$$\frac{di_{rq}}{dt} = -\frac{R_r}{\sigma L_r}i_{rq} - \omega_r\left(i_{rd} + \frac{L_m}{\sigma L_r L_s}\phi_s\right) + \frac{1}{\sigma L_r}v_{rq}, \tag{36}$$

$$\frac{di_{rd}}{dt} = -\frac{1}{\sigma L_r}\left(R_r + \frac{R_s L_m^2}{L_s^2}\right)i_{rd} + \omega_r i_{rq} + \frac{L_m R_s}{\sigma L_r L_s^2}\phi_s + \frac{1}{\sigma L_r}v_{rd}, \tag{37}$$

$$\frac{d\phi_s}{dt} = -\frac{R_s}{L_s}\phi_s + \frac{R_s L_m}{L_s}i_{rd}. \tag{38}$$

Here, $T_{em} = -p_r\phi_s\frac{L_m}{L_s}i_{rq}$, as indicated by (17). The active and reactive powers, represented by (18) and (19), are reformulated as

$$P_s = -v_s\frac{L_m}{L_s}i_{rq}, \tag{39}$$

$$Q_s = \frac{v_s}{L_s}(\phi_s - L_m i_{rd}). \tag{40}$$

In this case, $v_s = \omega_s\phi_s - \frac{R_s L_m}{L_s}i_{rq}$. Note that if R_s is assumed to be approximately zero, then $\frac{d\phi_s}{dt} \approx 0$, and the dynamics become identical to those presented in [23]. In this paper, however, R_s is non-zero, and ϕ_s is a time-varying signal governed by (38).

3. Design of Output Feedback Controllers

The state-space equations include two control inputs, v_{rq} and v_{rd}. The primary control objective is to drive ω to ω_d for optimal power extraction from the wind turbine. The secondary objective is to regulate reactive power Q_s to zero. From Equations (35)–(38), it is evident that the second-order derivative of ω is a function of v_{rq}, and the first-order time derivative of Q_s involves v_{rd}. Based on these observations, the following dynamic equations are formulated:

$$\ddot{\omega} = f_1(v_{rq}, t), \tag{41}$$

$$\dot{Q}_s = f_2(v_{rd}, t), \tag{42}$$

where functions $f_1(\cdot)$ and $f_2(\cdot)$ are considered to be unknown. These functions are explicit functions of time t, and may involve state variables ($\omega(t)$, $i_{rd}(t)$, $i_{rq}(t)$, $\phi_s(t)$) as well as time-varying parameters, external disturbances, and measurement errors that are difficult to model precisely. It is also inferred that the inputs v_{rq} and v_{rd} can be employed to control $\omega(t)$ and $Q_s(t)$ independently. That is, these inputs and outputs are decoupled, enabling the independent design of two controllers. Subsequent subsections present the design of control laws to achieve these objectives.

In what follows, the two-norm of vector $\mathbf{x}$ is denoted by $|\mathbf{x}|$, and the absolute value of the scalar v is also indicated by $|v|$. Notation $a(t) \to 0$ is employed to signify $\lim_{t\to\infty} a(t) = 0$, indicating that $a(t)$ converges to zero as t approaches infinity. Similarly, $a(t) \to b(t)$ denotes that $a(t)$ asymptotically approaches $b(t)$ as t approaches infinity, or $\lim_{t\to\infty} a(t) = b(t)$.

3.1. MPPT Control

In this paper, the differentiator-based output feedback control scheme, as discussed in the introduction and detailed in [21,22,35], is employed for MPPT control of the WECS as represented by Equations (35)–(38). It is evident that the relative degree between the outputs ω and v_{rd} is two, as v_{rd} first appears in the second-order time derivative of ω. To construct the feeding signal $a_1(t)$ for the higher-order switching differentiator (HOSD), a second-order linear filter is required, as given by

$$\begin{aligned} \dot{w}_{11} &= -w_{11} + w_{12}, \\ \dot{w}_{12} &= -w_{12} + v_{rq}. \end{aligned} \tag{43}$$

Here, w_{11} and w_{12} are the state variables of the Linear Time-Invariant (LTI) filter (43). Wedefine the tracking error e_1 as

$$e_1 = (\omega - \omega_d)g_1, \tag{44}$$

where $g_1 > 0$ is a gain constant to be determined. Subsequently, signal $a_1(t)$ is given by

$$a_1(t) = e_1 - w_{11}. \tag{45}$$

To formulate the control law, the following HOSD is introduced, as per [21,35]:

Lemma 1. *Let $a_1(t)$ be a signal whose time derivatives are piecewise-bounded, such that $|\dot{a}_1| \leq L_{11}^*$ and $|\ddot{a}_1| \leq L_{12}^*$, for some positive constants L_{11}^*, L_{12}^*. Consider dynamics*

$$\left. \begin{array}{l} \dot{\alpha}_{11} = 10L_1\epsilon_{11} + \sigma_{11} \\ \dot{\sigma}_{11} = L_1 \operatorname{sgn}(\epsilon_{11}) \end{array} \right\}, \tag{46}$$

$$\left. \begin{array}{l} \dot{\alpha}_{12} = 7L_1\epsilon_{12} + \sigma_{12} \\ \dot{\sigma}_{12} = L_1 \operatorname{sgn}(\epsilon_{12}) \end{array} \right\}, \tag{47}$$

where $\epsilon_{11} = a_1(t) - \alpha_{11}$ and $\epsilon_{12} = \sigma_{11} - \alpha_{12}$. If L_1 is chosen sufficiently large such that $L_1 > \max\{L_{11}^*, L_{12}^*\}$, then $\sigma_{11} \to \dot{a}_1$ and $\sigma_{12} \to \ddot{a}_1$.

The comprehensive proof is presented in [33]. From Lemma 1, the following equations hold:

$$\begin{aligned} \sigma_{11} &= \dot{a}_1 + \delta_{11}(t) \\ &= \dot{e}_1 - \dot{w}_{11} + \delta_{11}(t) \\ &= \dot{e}_1 + w_{11} - w_{12} + \delta_{11}(t), \end{aligned} \tag{48}$$

$$\begin{aligned} \sigma_{12} &= \ddot{a}_1 + \delta_{12}(t) \\ &= \ddot{e} + \dot{w}_{11} - \dot{w}_{12} + \delta_{12}(t) \\ &= \ddot{e} - w_{11} + 2w_{12} - v_{rq} + \delta_{12}(t), \end{aligned} \tag{49}$$

where $\delta_{11}(t)$ and $\delta_{12}(t)$ are asymptotically vanishing estimation errors; that is, $\delta_{11}(t) \to 0$ and $\delta_{12}(t) \to 0$. If the error vector is defined as $\mathbf{e}_1 = [e_1, \dot{e}_1]^T$, its estimate can be determined from Equation (48) as follows:

$$\hat{\mathbf{e}}_1 = \begin{bmatrix} e \\ \sigma_{11} - w_{11} + w_{12} \end{bmatrix}. \tag{50}$$

Subsequently, the output feedback control input v_{rq} is proposed as

$$v_{rq} = -\sigma_{12} - (w_{11} - 2w_{12}) - \mathbf{k}_1^T \hat{\mathbf{e}}_1, \tag{51}$$

where $\mathbf{k}_1 = [k_{11}, k_{12}]^T$ is determined so that the polynomial $s^2 + k_{12}s + k_{11}$ is Hurwitz.

Theorem 1. *The control input v_{rq} given by (51), in conjunction with the HOSD as described in Lemma 1, and the LTI filter (43) ensures that ω asymptotically tracks ω_d.*

Proof. From Equations (51) and (49), the following equality can be straightforwardly derived:

$$\begin{aligned} v_{rq} &= -\sigma_{12} - (w_{11} - 2w_{12}) - \mathbf{k}_1^T \hat{\mathbf{e}}_1 \\ &= -(\ddot{e}_1 - w_{11} + 2w_{12} - v_{rq} + \delta_{12}(t)) \\ &\quad -(w_{11} - 2w_{12}) - \mathbf{k}_1^T \mathbf{e}_1 - k_{12}\delta_{11}(t) \\ &= -\ddot{e}_1 + v_{rq} - \mathbf{k}_1^T \mathbf{e}_1 - \delta_{12}(t) - k_{12}\delta_{11}(t). \end{aligned} \tag{52}$$

Defining $d_1(t) = -\delta_{12}(t) - k_{12}\delta_{11}(t)$, we can induce

$$\ddot{e}_1 = -\mathbf{k}_1^T \mathbf{e} + d_1(t). \tag{53}$$

This can be rewritten in vector form as

$$\dot{\mathbf{e}}_1 = \mathbf{A}\mathbf{e}_1 + \mathbf{b}d_1(t), \tag{54}$$

where

$$\mathbf{A} = \begin{bmatrix} 0 & 1 \\ -k_{11} & -k_{12} \end{bmatrix}, \mathbf{b} = \begin{bmatrix} 0 \\ 1 \end{bmatrix}. \tag{55}$$

Positive definite matrices $\mathbf{P}$ and $\mathbf{Q}$ exist such that $\mathbf{A}^T\mathbf{P} + \mathbf{P}\mathbf{A} + \mathbf{Q} = 0$. The time derivative of the Lyapunov function $V_1 = \mathbf{e}_1^T\mathbf{P}\mathbf{e}_1$ is given by

$$\begin{aligned} \dot{V}_1 &= -\mathbf{e}_1^T\mathbf{Q}\mathbf{e}_1 + 2\mathbf{e}_1^T\mathbf{P}\mathbf{b}d_1(t) \\ &\leq -\lambda_{min}(\mathbf{Q})|\mathbf{e}_1|^2 + 2|\mathbf{e}_1|\lambda_{max}(\mathbf{P})|d_1(t)|, \end{aligned} \tag{56}$$

where $\lambda_{\min}(\cdot)$ and $\lambda_{\max}(\cdot)$ denote the minimum and maximum eigenvalues of a matrix, respectively. From this inequality, it follows that if $|\mathbf{e}_1| > \mu|d_1(t)|$, where $\mu = \frac{2\lambda_{\max}(\mathbf{P})}{\lambda_{\min}(\mathbf{Q})}$, then $\dot{V}_1 < 0$. Given that $d_1(t)$ converges to zero asymptotically, it can be concluded that $|\mathbf{e}_1|$ is also asymptotically stable. $\square$

3.2. Regulating Q_s to Zero

The second control objective outlined in [23] involves regulating the reactive power Q_s to zero using v_{rd}. The relative degree between the output Q_s and the input v_{rd} is one, simplifying the control law compared to the MPPT control law discussed in the preceding subsection. To generate the feeding signal $a_2(t)$ for the second HOSD, we adopt the following first-order linear filter:

$$\dot{w}_{21} = -w_{21} + v_{rd}, \tag{57}$$

where w_{21} is a state variable of this filter. We let the tracking error be defined as

$$e_2 = (Q_s - 0)g_2. \tag{58}$$

Here, $g_2 > 0$ is a tunable amplification parameter. Signal $a_2(t)$ is then given by

$$a_2(t) = e_2 - w_{21}. \tag{59}$$

We introduce the following HOSD that is capable of observing $\dot{Q}_s$.

Lemma 2 ([36]). *Let $a_2(t)$ be a signal whose time derivatives are bounded in the piecewise sense such that $|\dot{a}_2| \leq L_2^*$ for some positive constants L_2^*. Consider the following dynamics:*

$$\left. \begin{aligned} \dot{\alpha}_{21} &= 10L_2\epsilon_{21} + \sigma_{21} \\ \dot{\sigma}_{21} &= L_2\,\mathrm{sgn}(\epsilon_{21}), \end{aligned} \right\} \tag{60}$$

where $\epsilon_{21} = a_2(t) - \alpha_{21}$. If L_2 is chosen sufficiently large such that $L_1 > L_2^*$, then $\sigma_{21} \to \dot{a}_2$.

The detailed proof is presented in [33]. From Lemma 2, the following equation holds:

$$\begin{aligned} \sigma_{21} &= \dot{a}_2 + \delta_{21}(t) \\ &= \dot{e}_2 - \dot{w}_{21} + \delta_{21}(t) \\ &= \dot{e}_2 + w_{21} - v_{rd} + \delta_{21}(t), \end{aligned} \tag{61}$$

where $\delta_{21}(t)$ is asymptotically vanishing estimaion error, i.e., $\delta_{21}(t) \to 0$. Then, the control input v_{rd} is proposed as

$$v_{rd} = -\sigma_{21} + w_{21} - k_2 e_2, \tag{62}$$

where $k_2 > 0$ is a design constant.

Theorem 2. *The control input v_{rd} as described in (62), in conjunction with HOSD (2) and the LTI filter (57), ensures that the reactive power $Q_s(t)$ asymptotically converges to zero.*

Proof. The following equality can be straightforwardly derived from Equations (62) and (61):

$$\begin{aligned} v_{rd} &= -\sigma_{21} + w_{21} - k_2 e_2 \\ &= -(\dot{e}_2 + w_{21} - v_{rd} + \delta_{21}(t)) + w_{21} - k_2 e_2 \\ &= -\dot{e}_2 + v_{rd} - k_2 e_2 - \delta_{21}(t). \end{aligned} \tag{63}$$

From the last equality, the following relationship is deduced:

$$\dot{e}_2 = -k_2 e_2 - \delta_{21}(t). \tag{64}$$

We let $V_2 = \frac{e_2^2}{2k_2}$ serve as the second Lyapunov function. Its time derivative is

$$\begin{aligned} \dot{V}_2 &= e_2 \frac{\dot{e}_2}{k_2} \\ &= -e_2^2 - e_2 \frac{\delta_{21}(t)}{k_2} \\ &\leq -|e_2|^2 + |e_2| \frac{|\delta_{21}(t)|}{k_2}. \end{aligned} \tag{65}$$

This implies that if $|e_2| > \frac{|\delta_{21}(t)|}{k_2}$, then $\dot{V}_2 < 0$. Given that $\delta_{21}(t)$ converges to zero asymptotically, $|e_2|$ also asymptotically converges to zero. $\square$

Remark 1. *It is worth noting that the proposed control scheme does not require information about system parameters or nonlinear functions in the WECS dynamics. Only measured values (v_w, ω, and Q_s) and the information about λ^* to calculate ω_d are needed. Other details such as the exact structure of the $C_p(\cdot)$ function, precise system parameters, and the configuration of the dynamic equations are not necessary for the formulation of control laws. Moreover, the control strategy is robust to unknown or varying system parameters and unmodeled dynamic structures within the WECS.*

Remark 2. *The proposed controller, based on differentiator-based control techniques, shares similar advantages with data-driven control [37] in that it does not require a precise dynamic model of the system under control. However, while data-driven control involves an identification process based on observed system behavior data, differentiator-based control eliminates the need for such an identification phase. It enables the immediate design of output feedback controllers using minimal information, such as relative degree and control direction.*

4. Simulations

In this section, the effectiveness of the proposed control strategy is validated through simulations using a 1.5 MW DFIG-WECS model as described in [23]. All simulations were conducted using Python libraries, specifically NumPy, SciPy, and Matplotlib [38]. The parameters relevant to this WECS model are provided in Table 2, while the design parameters of the proposed controllers are detailed in Table 3. In addition to the proposed controller, simulation experiments were also conducted using a PI controller to compare performance. The control equations for the PI controller are as follows:

$$v_{rq} = 1000e_1 + 200 \int_0^t e_1 \, dt, \tag{66}$$

$$v_{rd} = 1000e_2 + 200 \int_0^t e_2 \, dt. \tag{67}$$

Here, the error signals e_1 and e_2 are defined as in Equations (44) and (58), respectively, with the values of g_1 and g_2 as given in Table 3. The gains for the PI controller were selected empirically through multiple simulation runs, prioritizing output tracking performance over transient response.

Table 2. Parameters of WECS.

Notation	Value	Description
c_1	0.5176	constant in (3)
c_2	116	constant in (3)
c_3	0.4	constant in (3)
c_4	5	constant in (3)
c_5	21	constant in (3)
c_6	0.0068	constant in (3)
ω_s	100π	stator electrical angular speed
R_s	0.005	stator resistance
R_r	0.228	rotor resistance
L_s	0.407	stator inductance
L_r	0.299	rotor inductance
L_m	0.0016	mutual inductance
p_r	4	number of pole pairs
J	4.4532×10^5	total inertia
D	400	damping constant
ρ	1.08	air density
R	35	radius of the blade
n_g	43.165	gear ratio
λ^*	8.1072	optimal value of λ

Table 3. Design parameters of the controllers.

Notation	Value	Description
L_1	1000	constant in (46) and (47)
g_1	20000	constant in (44)
$\mathbf{k}_1$	$[10^6, 2000]^T$	vector in (51)
L_2	1000	constant in (60)
g_2	300	constant in (58)
k_2	1000	constant in (62)

As demonstrated in Figure 4, the wind speed model incorporates both variability and rapid fluctuations, providing a realistic test scenario for evaluating the proposed control scheme. As the machinery operates over an extended period, factors such as wear and tear can lead to changes in inertia coefficients or damping constants. Additionally, variations in ambient temperature can alter the resistance and inductance of the generator. To showcase the controller's performance, a simulation was executed where the constants J, D, R_s, R_r, L_s, L_r, and L_m were changed by an extreme 40% at the 100 s mark, and the results were presented to illustrate its robustness under such conditions.

Figure 5 depicts the $\omega(t)(= y_1)$ along with its desired value $\omega_d(t)$, illustrating rapid and accurate tracking performance of the proposed controller. Moreover, the transient response of the proposed controller is significantly better compared to that of the PI controller. The output tracking performance of the proposed controller closely aligns with $\omega_d(t)$, whereas the PI controller struggles to accurately track $\omega_d(t)$ at inflection points.
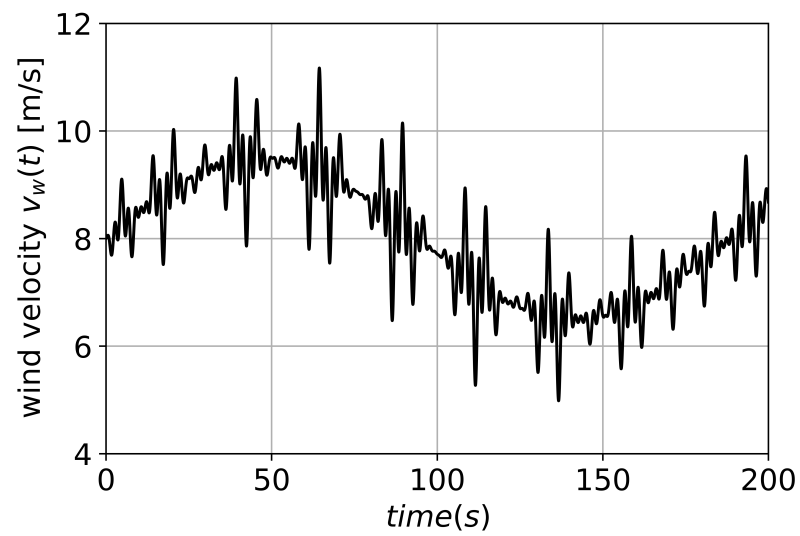
Figure 4. Waveform of the quickly varying wind speed $v_w(t)$ used in the simulation.
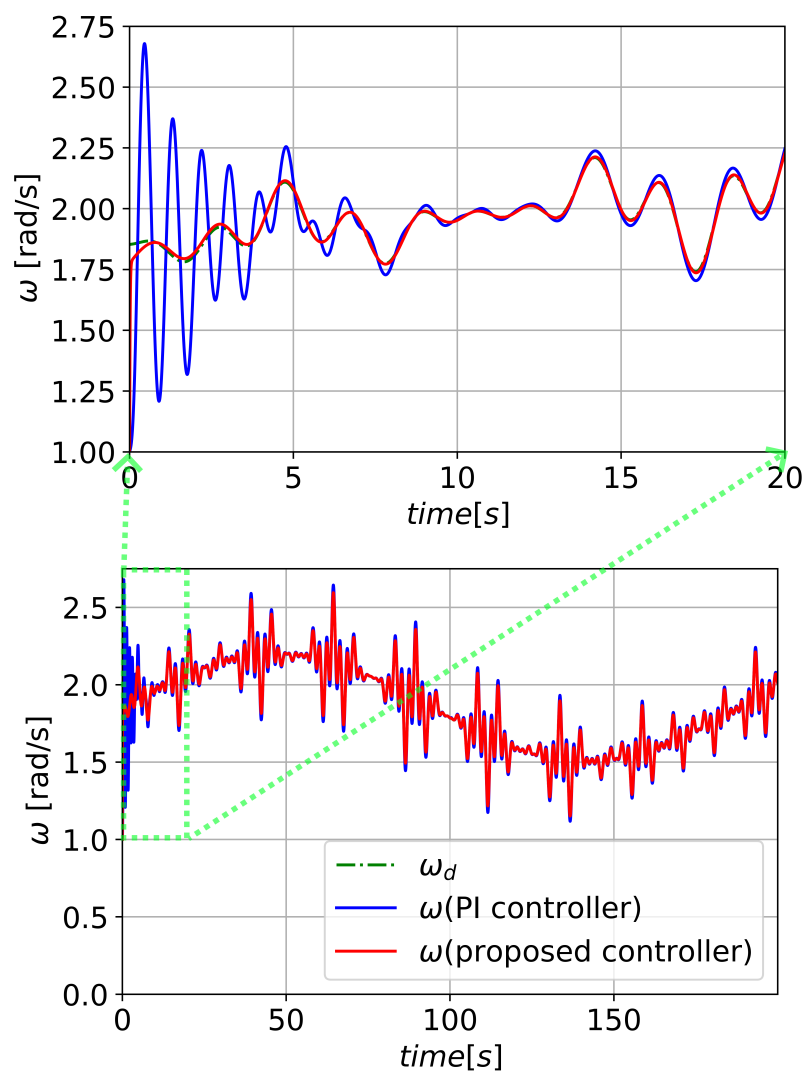

Figure 5. Trajectories of $\omega(t)$ and $\omega_d(t)$.

Figure 6 presents the regulating performance for reactive power $Q_s(= y_2)$, confirming the controller's ability to regulate Q_s to zero effectively. In these results, the proposed controller stands out for its oscillation-free transient response and more pronounced regulation performance. Additionally, as can be seen in Figure 5, both controllers exhibit insensitivity to parameter variations in ω at $t = 100$ s, while Q_s experiences a spike before immediate return to proper regulation. Figure 7 shows the actual power coefficient $Cp(\lambda, 0)$, which almost perfectly tracks the optimal command $Cp(\lambda^*, 0) \approx 0.48$ by the proposed controller. In contrast, the PI controller exhibits significant oscillations in its transient response and shows inferior steady-state performance. In Figure 8, the trajectories of the active power P_s are depicted, and Figure 9 illustrates the control voltage inputs v_{rd} and v_{rq}. In Figure 9a, it can be observed that the control inputs v_{rd} for both the PI and the proposed controllers are sensitive to the parameter value change occurring at 100 s, leading to spikes in Q_s at that moment.
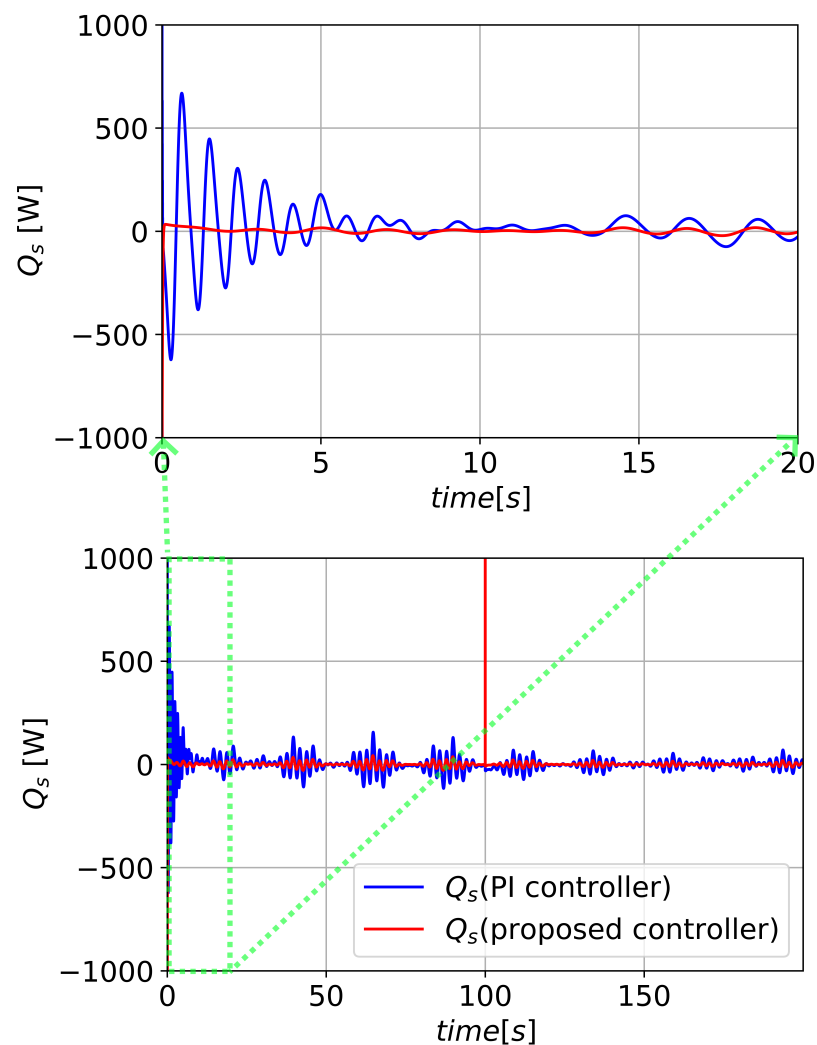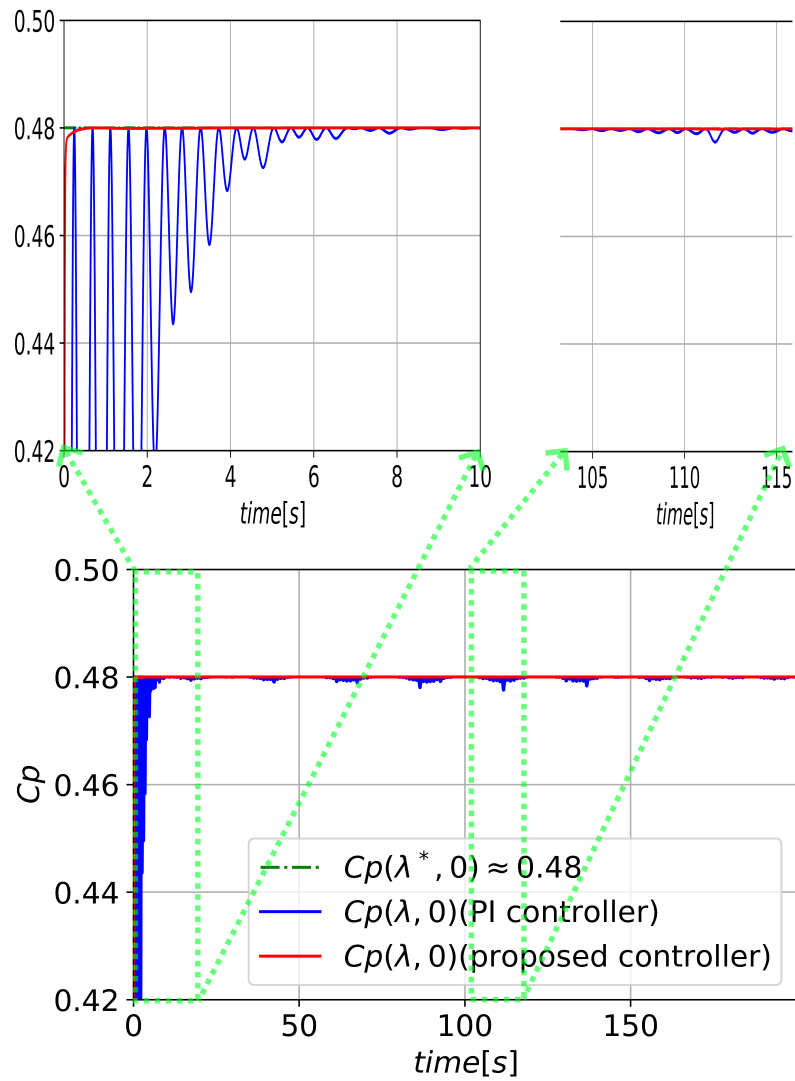

Figure 6. Trajectories of $Q_s(t)$.

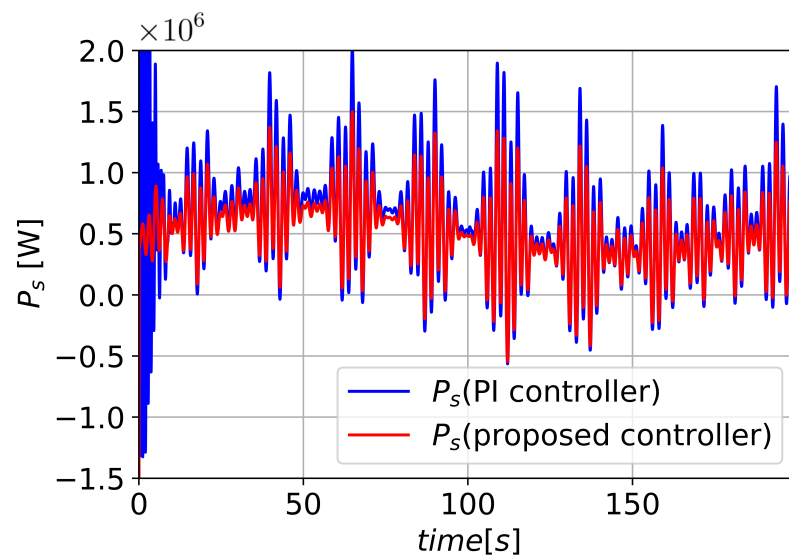**Figure 7.** Trajectory of $Cp(\lambda, 0)$.

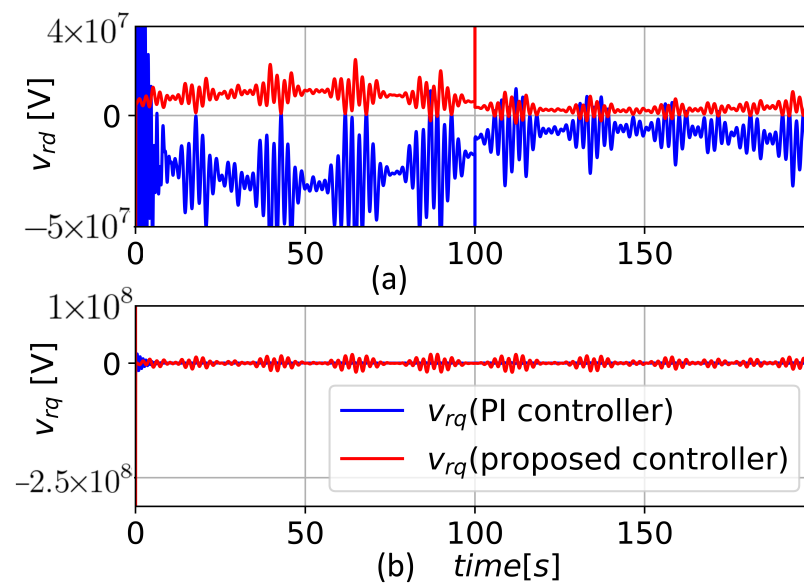**Figure 8.** Trajectories of $P_s(t)$.

Figure 9. Trajectories of (**a**) v_{rd} and (**b**) $v_{rq}(t)$.

5. Conclusions

This paper presents a novel differentiator-based MPPT controller for WECS equipped with DFIG. The work builds upon existing control algorithms [21,22] and offers several advantages, such as reduced reliance on detailed system information and enhanced robustness to parameter variations and disturbances. Specifically, our approach eliminates the necessity for explicit functional expressions or parameter values in the dynamic equations of the system, focusing instead solely on relative degrees and control directions. Employing HOSD to overestimate the time derivatives of system outputs, our methodology facilitates both a simplified controller architecture and a more straightforward stability analysis. In comparison with existing research, the proposed controller is distinguished by its minimal information requirements, simplified control law structures, systematic design approach, and a reduced number of design constants. Simulation results substantiate the effectiveness of the proposed control algorithm in both tracking maximum power and asymptotically regulating the reactive power to zero. Overall, this contribution offers a more efficient and less complicated approach to MPPT control in WECS.

The differentiator-based controller proposed in this paper is considered to be directly applicable to the MPPT control of permanent magnet synchronous generator WECS, and this is reserved as a topic for future research. One limitation of the proposed controller is that it requires measurements of both the system output and wind speed. Therefore, subsequent research should focus on developing controller strategies that eliminate the need for wind speed sensors.

Data Availability Statement: No new data were created or analyzed in this study. Data sharing is not applicable to this article.

Conflicts of Interest: The author declares no conflict of interest.

References

1. Cardenas, R.; Pena, R.; Alepuz, S. Overview of control systems for the operation of DFIGs in wind energy applications. *IEEE Trans. Ind. Electron.* **2013**, *60*, 2776–2798. [CrossRef]
2. Jadhav, H.T.; Roy, R. A comprehensive review on the grid integration of doubly fed induction generator. *Int. J. Electr. Power Energy Syst.* **2013**, *49*, 8–18. [CrossRef]
3. El-Naggar, M.F.; Mosaad, M.I.; Hasanien, H.M.; AbdulFattah, T.A.; Bendary, A.F. Elephant herding algorithm-based optimal PI controller for LVRT enhancement of wind energy conversion systems. *Ain Shams Eng. J.* **2021**, *12*, 599–608. [CrossRef]

4.   Mossad, M.I.; Sabiha, N.A.; Abu-Siada, A.; Taha, I.B.M. Application of Superconductors to Suppress Ferroresonance Overvoltage in DFIG-WECS. *IEEE Trans. Energy Convers.* **2021**, *37*, 766–777. [CrossRef]

5.   Hamane, B.; Doumbia, M.L.; Bouhamida, M.; Draou, A.; Chaoui, H.; Benghanem, M. Comparative study of PI, RST, sliding mode and fuzzy supervisory controllers for DFIG based wind energy conversion system. *Int. J. Renew. Energy Res.* **2015**, *5*, 1174–1185.

6.   Levant, A. Higher-order sliding modes, differentiation and output-feedback control. *Int. J. Control* **2003**, *76*, 924–941. [CrossRef]

7.   Levant, A.; Livne, M. Weighted Homogeneity and Robustness of Sliding Mode Control. *Automatica* **2016**, *72*, 186–193. [CrossRef]

8.   Tong, S.; Liu, C.; Li, Y. Fuzzy-adaptive decentralized output-feedback control for large-scale nonlinear systems with dynamical uncertainties. *IEEE Trans. Fuzzy Syst.* **2010**, *18*, 845–861. [CrossRef]

9.   Tong, S.C.; Li, Y.M.; Zhuang, H.-G. Adaptive neural network decentralized backstepping output-feedback control of nonlinear large-scale systems with time-delays. *IEEE Trans. Neural Netw.* **2011**, *22*, 1073–1086. [CrossRef]

10. Li, J.; Chen, W.; Li, J.-M. Adaptive NN output-feedback decentralized stabilization for a class of large-scale stochastic nonlinear strict-feedback systems. *Int. J. Robust Nonlinear Control* **2011**, *21*, 452–472. [CrossRef]

11. Tong, S.; Li, Y.; Liu, Y. Adaptive fuzzy output feedback decentralized control of pure-feedback nonlinear large-scale systems. *Int. J. Robust Nonlinear Control* **2014**, *24*, 930–954. [CrossRef]

12. Yang, Y.; Yue, D.; Xue, Y. Decentralized adaptive neural output feedback control of a class of large-scale time-delay systems with input saturation. *J. Frankl. Inst.* **2015**, *352*, 2129–2151. [CrossRef]

13. Jiang, X.; Mu, X.; Hu, Z. Decentralized Adaptive Fuzzy Tracking Control for a Class of Nonlinear Uncertain Interconnected Systems with Multiple Faults and DoS Attack. *IEEE Trans. Fuzzy Syst.* **2020**, *29*, 3130–3141. . [CrossRef]

14. Wang, H.; Xiaoping, P.; Bao, J.; Xie, X.-J.; Li, S. Adaptive Neural Output-Feedback Decentralized Control for Large-Scale Nonlinear Systems with Stochastic Disturbances. *IEEE Trans. Neural Netw. Learn. Syst.* **2020**, *31*, 972–983. [CrossRef] [PubMed]

15. Ma, Z.; Ma, H. Decentralized Adaptive NN Output-Feedback Fault Compensation Control of Nonlinear Switched Large-Scale Systems with Actuator Dead-Zones. *IEEE Trans. Syst. Man Cybern. Syst.* **2020**, *50*, 3435–3447. [CrossRef]

16. Wang, H.; Chen, B.; Lin, C.; Sun, Y. Neural-network-based decentralized output-feedback control for nonlinear large-scale delayed systems with unknown dead-zones and virtual control coefficients. *Neurocomputing* **2020**, *424*, 255–267. . [CrossRef]

17. Bechlioulis, C.P.; Rovithakis, G.A. A low-complexity global approximation-free control scheme with prescribed performance for unknown pure feedback systems. *Automatica* **2014**, *50*, 1217–1226. [CrossRef]

18. Zhang, J.-X.; Yang, G.-H. Low-Complexity Tracking Control of Strict-Feedback Systems with Unknown Control Directions. *IEEE Trans. Autom. Control* **2019**, *64*, 5175–5182. [CrossRef]

19. Zhang, J.-X.; Yang, G.-H.; Ding, W. Global Output-Feedback Prescribed Performance Control of Nonlinear Systems with Unknown Virtual Control Coefficients. *IEEE Trans. Autom. Control* **2022**, *67*, 6904–6911. [CrossRef]

20. Guo, Z.; Oliveira, T.R.; Guo, J.; Wang, Z. Performance-Guaranteed Adaptive Asymptotic Tracking for Nonlinear Systems with Unknown Sign-Switching Control Direction. *IEEE Trans. Autom. Control* **2023**, *68*, 1077–1084. [CrossRef]

21. Park, J.-H.; Kim, S.-H.; Park, T.-S. Approximation-Free Output-Feedback Non-Backstepping Controller for Uncertain SISO Nonautonomous Nonlinear Pure-Feedback Systems. *Mathematics* **2019**, *7*, 456. [CrossRef]

22. Park, J.-H.; Kim, S.-H.; Lee, D.-H. Decentralized Output-Feedback Controller for Uncertain Large-Scale Nonlinear Systems Using Higher-Order Switching Differentiator. *IEEE Access* **2021**, *9*, 21227–21235. [CrossRef]

23. Wang, J.; Bo, D.; Miao, Q.; Li, Z.; Wu, X.; Lv, D. Maximum power point tracking control for a doubly fed induction generator wind energy conversion system based on multivariable adaptive super-twisting approach. *Int. J. Electr. Power Energy Syst.* **2021**, *124*, 106347. [CrossRef]

24. Xiong, L.; Li, P.; Wu, F.; Ma, M.; Khan, M.W.; Wang, J. A coordinated high-order sliding mode control of DFIG wind turbine for power optimization and grid synchronization. *Int. J. Electr. Power Energy Syst.* **2019**, *105*, 679–689. [CrossRef]

25. Shihabudheen, K.V.; Raju, S.K.; Pillai, G.N. Control for grid-connected DFIGbased wind energy system using adaptive neuro-fuzzy technique. *Int. Trans. Electr. Energy Syst.* **2018**, *28*, e2526. [CrossRef]

26. Kumar, R.; Agrawal, H.P.; Shah, A.; Bansal, H.O. Maximum power point tracking in wind energy conversion system using radial basis function based neural network control strategy. *Sustain. Energy Technol. Assess.* **2019**, *36*, 100533. [CrossRef]

27. Aissaoui, H.E.; Ougli, A.E.; Tidhaf, B. Neural Networks and Fuzzy Logic Based Maximum Power Point Tracking Control for Wind Energy Conversion System. *Adv. Sci. Technol. Eng. Syst. J.* **2021**, *6*, 586–592. [CrossRef]

28. Sami, I.; Ullah, S.; Amin, S.U.; Al-Durra, A.; Ullah, N.; Ro, J.S. Convergence Enhancement of Super-Twisting Sliding Mode Control Using Artificial Neural Network for DFIG-Based Wind Energy Conversion Systems. *IEEE Access* **2022**, *10*, 97625–97641. [CrossRef]

29. Yan, S.; Gu, Z.; Park, J.H.; Xie, X. Adaptive Memory-Event-Triggered Static Output Control of T–S Fuzzy Wind Turbine Systems. *IEEE Trans. Fuzzy Syst.* **2022**, *30*, 3894–3904. [CrossRef]

30. Yan, S.; Gu, Z.; Park, J.H.; Xie, X. Sampled Memory-Event-Triggered Fuzzy Load Frequency Control for Wind Power Systems Subject to Outliers and Transmission Delays. *IEEE Trans. Cybern.* **2023**, *53*, 4043–4053. [CrossRef]

31. Jing, F.; Liu, W.; Sun, H.; Yu, F.; Wang, K. Prescribed performance finite-time control of wind energy conversion systems with input constraint and system uncertainty. *Int. Trans. Electr. Energy Syst.* **2021**, *32*, e13215. [CrossRef]

32. Lv, G.; Cong, S.; Liu, Y.; Peng, Z.; Wang, D. Maximum Power Tracking Control of Wind Energy Conversion Systems Based on Prescribed Performance Function and Extended State Observer. In Proceedings of the 2018 3rd International Conference on Advanced Robotics and Mechatronics (ICARM), Singapore, 18–20 July 2018; pp. 829–834. [CrossRef]

33. Park, J.-H.; Kim, S.-H.; Park, T.-S. Asymptotically Convergent Higher-Order Switching Differentiator. *Mathematics* **2020**, *8*, 185. [CrossRef]
34. Boukhezzar, B.; Siguerdidjane, H. Nonlinear control with wind estimation of a DFIG variable speed wind turbine for power capture optimization. *Energy Convers. Manag.* **2009**, *50*, 885–892. .: 10.1016/j.enconman.2009.01.011. [CrossRef]
35. Park, J.-H.; Kim, S.-H.; Park, T.-S. Differentiator-Based Output-Feedback Controller for Uncertain Nonautonomous Nonlinear Systems with Unknown Relative Degree. *IEEE Access* **2020**, *8*, 172593–172600. [CrossRef]
36. Park, J.-H.; Kim, S.-H.; Park, T.-S. Asymptotically convergent switching differentiator. *Int. J. Adapt. Control Signal Process.* **2019**, *33*, 557–566. [CrossRef]
37. Hou, Z.; Chi, R.; Gao, H. An Overview of Dynamic-Linearization-Based Data-Driven Control and Applications. *IEEE Trans. Ind. Electron.* **2017**, *64*, 4076–4090. [CrossRef]
38. Hunter, J.D. Matplotlib: A 2D graphics environment. *Comput. Sci. Eng.* **2007**, *9*, 90–95. [CrossRef]